



Cite this: *Nanoscale Horiz.*, 2025, 10, 3319

Received 21st July 2025,  
Accepted 11th September 2025

DOI: 10.1039/d5nh00519a

[rsc.li/nanoscale-horizons](http://rsc.li/nanoscale-horizons)

## Adaptive catalytic compartments emerge from synergistic integration of DNA nanostructures and transient coacervates

Abhay Srivastava, Parth Kumar, Mathesh Punugusamy, Sourav Das and Subinoy Rana \*

**Biomolecular condensates formed via liquid–liquid phase separation (LLPS) are essential to cellular organization, catalysis, and regulation of biochemical pathways. Inspired by such natural systems, we present a new adaptive coacervate formed by multivalent salt-bridge interactions of polyhexamethylene biguanide (PHMB) polymer and adenosine triphosphate (ATP). These phase separated compartments efficiently sequester guanine-rich DNA sequences that adopt G-quadruplex (GQ) conformations in the presence of potassium ions. Hemin intercalates into these GQ structures to produce a catalytically active DNAzyme with amplified peroxidase-like activity. Within the coacervate, reduced molecular diffusion and increased local substrate concentrations synergistically augment the catalytic efficiency of the DNAzyme by 10-fold compared to that in the unconfined state. Integrating an enzymatic degradation cycle by alkaline phosphatase allows ATP-fueled dissipative behavior of the coacervates. By integrating self-assembling catalytic motifs within a dissipative host environment, this system demonstrates key principles of spatially and temporally regulated catalysis, mimicking features of cellular microreactors. Our work highlights the potential of synthetic LLPS-based platforms as tunable and compartmentalized catalytic systems, with implications for biomimetic reactor design and the development of advanced functional materials.**

### 1. Introduction

Cells, the fundamental units of life, rely on a diverse array of spatiotemporal mechanisms to organize their biochemical activities.<sup>1,2</sup> Beyond the classical paradigm of membrane-bound organelles, an expanding base of research underscores the role of membraneless macromolecular condensates in dynamically orchestrating intracellular reactions, gene regulation, and stress responses.<sup>3–5</sup> These condensates act as arbiters

### New concepts

This work demonstrates a synthetic liquid–liquid phase separated (LLPS) microreactor that integrates self-assembling DNAzyme catalysts within dynamic coacervate compartments. We form adaptive coacervates via multivalent salt-bridge interactions between polyhexamethylene biguanide (PHMB) and ATP, which offer enhanced stability under physiologically relevant ionic strengths and greater directionality than electrostatic interactions. These coacervate microdroplets sequester guanine-rich DNA that folds into G-quadruplex structures in the presence of K<sup>+</sup> ions, into which hemin intercalates to form a DNAzyme with peroxidase-like activity. The synergy of slowed diffusion and high local substrate concentrations within the coacervate phase boosts the DNAzyme's catalytic efficiency by about 10-fold relative to the unconfined solution. Furthermore, coupling coacervate assembly to an ATP-degrading enzyme (alkaline phosphatase) yields a fuel-driven, dissipative system: coacervates form and sustain catalysis while ATP is supplied, and then dissipate as the fuel is consumed. Together, these results combine dynamic phase-separated hosts with programmable enzymatic control to establish a proof-of-concept for programmable catalytic compartments. This demonstrates that salt-bridge-mediated LLPS can be exploited to achieve spatiotemporally regulated, compartmentalized catalysis in synthetic systems, reminiscent of cellular microreactors.

of cellular biochemistry by the sequestration of molecules, the compartmentalization of reactions, and the facilitation of enhanced catalytic activity.<sup>6–8</sup> The study of such systems has emerged as a transformative field in modern cell biology and biochemistry, offering profound insights into the organizational principles that govern life at the molecular level.<sup>9</sup> At the heart of condensate formation lies a phenomenon known as liquid–liquid phase separation (LLPS), a process in which mixtures of macromolecules spontaneously demix from the surrounding solution to form dense, droplet-like phases that coexist with the more dilute cytoplasmic or nucleoplasmic environment.<sup>10,11</sup> This demixing is driven by a delicate balance of multivalent supramolecular interactions, including electrostatic interactions, hydrogen bonds, and hydrophobic contacts among macromolecular polymers like proteins and nucleic

Materials Research Centre, Indian Institute of Science, C. V. Raman Road, Bangalore, 560012, Karnataka, India. E-mail: subinoy@iisc.ac.in; Tel: +91 80 22932914

acids.<sup>12–15</sup> The microenvironment of these self-assembled systems possesses physico-chemical profiles distinct from the surrounding cellular milieu.<sup>16</sup> Several properties, including viscosity, pH, and molecular crowding, can be readily tuned within these condensates to facilitate selective partitioning of molecules and the regulation of biochemical kinetics.<sup>17–19</sup> For instance, nucleolar condensates maintain internal pH gradients that influence RNA processing and shape the behavior of other small molecules.<sup>20</sup>

The remarkable properties of macromolecular condensates in living cells have inspired the creation of coacervates as artificial condensates, which serve as versatile platforms to mimic and study the principles of cellular compartmentalization outside biological systems.<sup>21–25</sup> Much like their biological counterparts, coacervates are membraneless but robust droplets formed as a result of LLPS, often by mixing oppositely charged polymers, peptides, or even small molecules.<sup>26–29</sup> Coacervates have dense, crowded microenvironments and can serve as dynamic compartments capable of sequestering molecules and augmenting reaction rates by increasing local concentrations.<sup>30,31</sup> These phases are easily engineered to exhibit responsiveness to stimuli like pH, temperature, ionic strength, and redox state by modulating the underlying non-covalent interactions.<sup>32–35</sup> Such reversible self-assembly and dissipation mimics the tunable, adaptive nature of cellular condensates.<sup>36</sup> Coacervate systems are of increasing interest in synthetic biology and origin-of-life studies,<sup>37–39</sup> as they offer insight into prebiotic organization and enable the rational design of biomimetic platforms for applications like catalysis, bio-sensing, and drug delivery.<sup>40–43</sup> By and large, synthetic coacervates are formed through electrostatically driven self-assembly involving polycations (protamine, poly-L-lysine, diethylaminoethyl-dextran, chitosan, and polyarginine) and polyanions (chondroitin sulphate, polystyrene sulfonate, dextran sulphate, and heparin).<sup>44–50</sup> However, the lack of precise control and stability restricts their functional versatility. An effective strategy to mitigate this is to introduce salt-bridge interactions between the interacting molecules, which involve both electrostatic interactions and hydrogen bonding. This approach enhances both stability and biological relevance, as demonstrated in supramolecular assemblies like enzyme-modulating molecular glues<sup>51</sup> and tissue-adherent bioorganic nanoparticles.<sup>52</sup> These mechanisms closely resemble interactions within biological condensates like nucleoli, P-bodies, and stress granules, where multivalent interactions – including salt bridges between charged amino acid residues – play a critical role in phase separation and structural stability.<sup>53–55</sup>

While salt bridge-mediated catalytic assemblies are known to enhance activity inside confinement,<sup>56,57</sup> oligonucleotide catalysts inside coacervates are non-existent. While catalytic RNA molecules called ribozymes have long been known to exhibit catalytic functions in biological systems, recent advances have shown that single-stranded DNA can also fold into three-dimensional structures and act as a catalytic DNAzyme.<sup>58</sup> Among these, G-quadruplex DNA (GQ-DNA), a higher-order assembly of guanine-rich sequence stabilized by

Hoogsteen-type non-canonical hydrogen bonding and monovalent cations such as  $K^+$ ,<sup>59</sup> has garnered significant attention.<sup>60</sup> GQ-DNA not only serves as a robust, self-assembling scaffold but can leverage  $\pi$ - $\pi$  stacking to stabilize and orient cofactors like hemin with intrinsic peroxidase-like activity, which is typically unstable in aqueous environments.<sup>61</sup> The interaction of hemin with GQ-DNA enhances its catalytic performance, and hence the entire assembly functions in a manner analogous to a DNAzyme.<sup>61–63</sup> The potent ability of coacervates to amplify the functional activity of biomolecules could be utilized in augmenting the catalysis of DNAzymes. In this work, we present a novel coacervate system based on cationic polyhexamethylene biguanide (PHMB) and adenosine triphosphate (ATP) exploiting salt-bridge interactions between the biguanide and phosphate functional groups. While several existing coacervate systems have leveraged electrostatic interactions between polyelectrolytes and small molecules, our approach involves a distinct mode of interaction through salt-bridge formation, offering a new handle for tuning phase behavior. These PHMB-ATP coacervates (PA-Coa) exhibit hallmarks of non-equilibrium assemblies, including temporal evolution, responsiveness, and enzyme-mediated dissipativeness *via* ATP hydrolysis by the alkaline phosphatase (ALP) enzyme. We further demonstrate the facile partitioning of anionic GQ-DNA into the coacervate microenvironment, and the efficient co-localization of hemin with consequent enhanced peroxidase-like activity within the droplets, underscoring the role of compartmentalization in regulating catalysis. The PA-Coa system represents an advanced scaffold for designing non-equilibrium, adaptable compartments. By orchestrating the spatial organization of catalytic components within a confined, tunable environment, we recapitulate key features of cellular biochemistry and pave the way for the rational design of functional synthetic condensates.

## 2. Results and discussion

### 2.1 Fabrication of coacervates using salt-bridge interactions

In this work, we sought to fabricate a coacervate microdroplet by harnessing strong salt-bridge interactions between PHMB, a cationic antimicrobial polymer, and ATP, a biologically ubiquitous anion. The molecular structure of PHMB features two key elements: (i) biguanide groups that have the ability to establish potent electrostatic interactions with the negatively charged phosphate groups of ATP, and (ii) short aliphatic hydrophobic chains that provide molecular flexibility. The mixture of PHMB and ATP in water at 25 °C was initially transparent, which became turbid within a minute (Fig. 1a), indicating the formation of phase-separated structures. We constructed a phase diagram of PHMB and ATP coacervation by measuring the turbidity of solutions containing different ratios of the components, which revealed a distinct region where coacervate formation occurred (Fig. 1b). For further studies, we selected a ratio at which a significantly stable coacervation happens ( $C_{PHMB} = 1 \text{ mg mL}^{-1}$  and  $C_{ATP} = 2 \text{ mM}$ ). Importantly, this PA-

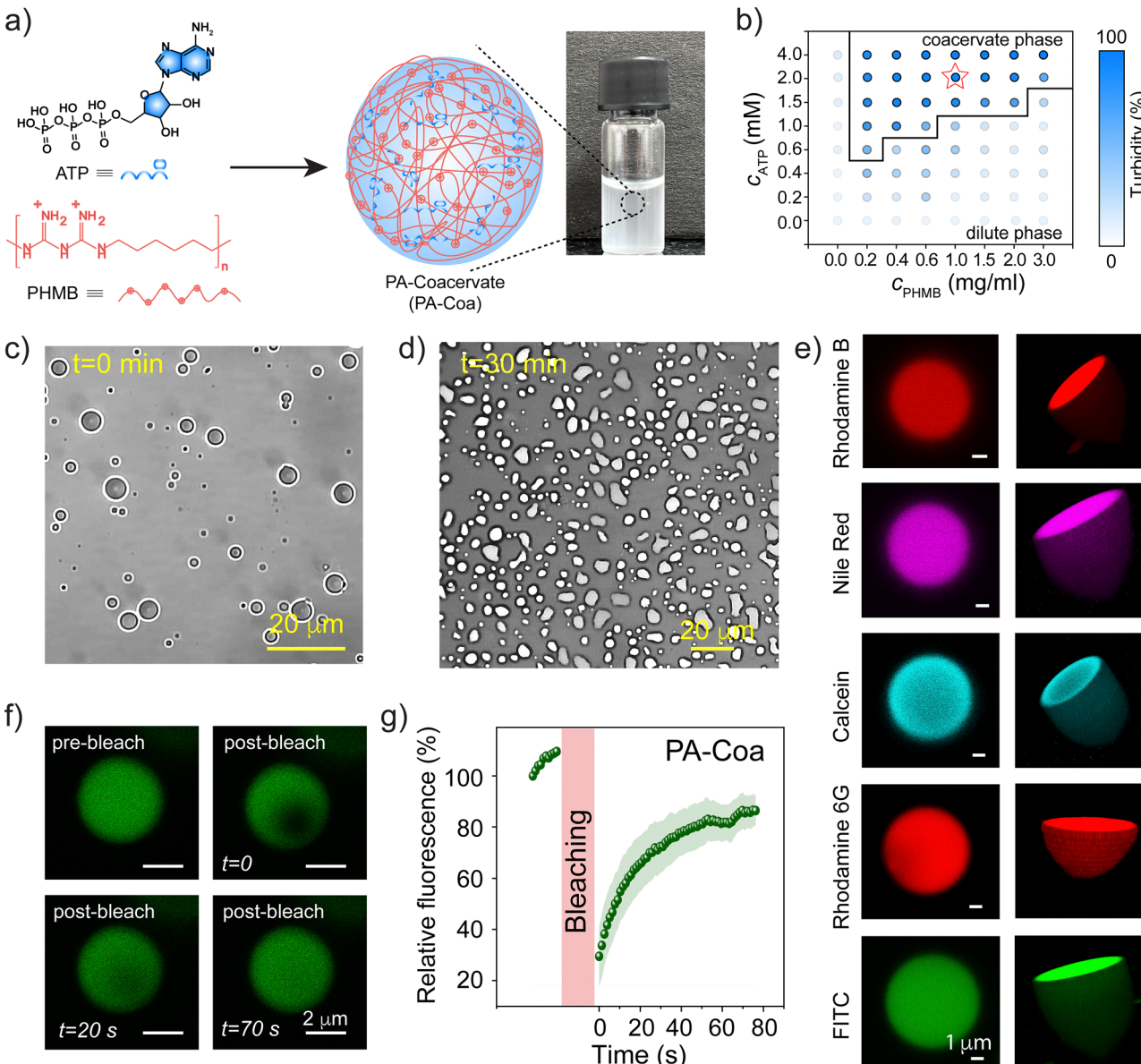


**Fig. 1** Formation and characterization of PHMB/ATP coacervates. (a) Schematic illustration of PA-Coa synthesis using a cationic PHMB polymer and nucleotide adenosine triphosphate (ATP). PA-Coa formed through electrostatic and hydrogen-bonding interactions. (b) A PA-Coa phase diagram constructed from transmittance measurements at 25 °C across varying ATP : PHMB concentration ratios. The red  $\star$  indicates the concentration chosen for subsequent experiments at  $C_{\text{PHMB}} = 1 \text{ mg mL}^{-1}$  and  $C_{\text{ATP}} = 2 \text{ mM}$ , and the black outline denotes the coexistence boundary defined by turbidity  $\geq 50\%$ , separating the dilute phase. (c) Optical microscopy image showing the formation of PA-Coa microdroplets. (d) Representative optical images showing the coalescence of PA-Coa. (e) Confocal fluorescence images of PA-Coa encapsulating various small molecules: Rhodamine B, Nile Red, calcein, Rhodamine 6G, and FITC. The right column shows 3D reconstructions from the corresponding z-stack images. Scale bars: 1  $\mu\text{m}$ . (f) Fluorescence recovery after photobleaching (FRAP) images of FITC-loaded PA-Coa. (g) Relative fluorescence recovery kinetics of PA-Coa following photobleaching. The data represent mean  $\pm$  SD from  $n = 3$  independent measurements. The shaded regions represent the error bars.

Coa demonstrates robust stability, remaining within the coacervate phase across a broad range of ionic strengths of 300 mM NaCl (Fig. S1) and temperatures up to 70 °C (Fig. S2). Optical microscopic images confirmed the formation of spherical droplets measuring  $\sim 2\text{--}5 \mu\text{m}$  in diameter (Fig. 1c). Dynamic light scattering measurements further validated these size estimates (Fig. S3). These PA-Coa exhibited hallmark properties, a characteristic of liquid-like coacervates, such as coalescence and a change in shape upon interaction (Fig. 1d),

aligning with dynamic properties observed in systems formed through LLPS.

A core feature underpinning the function of coacervate systems is their ability to sequester and concentrate a wide range of guest molecules from the surrounding medium. This is particularly significant for applications in catalysis, as it facilitates the local enrichment of reactants to attain concentrations sufficient to drive chemical reactions that would otherwise proceed sluggishly, or not at all, under dilute conditions.

We used a range of fluorescent dyes with varying charge states and hydrophobicity profiles, such as Rhodamine B (cationic, hydrophilic), Nile Red (neutral, hydrophobic), calcein (anionic, hydrophilic), Rhodamine 6G (cationic, hydrophobic) and FITC (anionic, hydrophobic), to evaluate the molecular uptake and compartmentalization efficiency of our PA-Coa system. Effective encapsulation within the droplets was demonstrated by the strong fluorescence signals displayed by each dye (Fig. S4–S8). Furthermore, z-stacked 3D confocal laser scanning microscopic (CLSM) images revealed that the fluorescence was uniformly distributed throughout the interior of the droplets, confirming that the dyes accumulated inside the coacervates as opposed to merely adsorbing to their surfaces (Fig. 1e). To further assess the dynamicity and fluidity of the spherical PA-Coa, we performed fluorescence recovery after photobleaching (FRAP) experiments, which showed rapid fluorescence recovery ( $\sim 85\%$  within 80 s) (Fig. 1f and g), indicative of high molecular mobility. These observations suggest that the PA-Coa droplets formed *via* LLPS provide a spatially uniform and chemically versatile microenvironment capable of encapsulating a wide variety of molecular species.

## 2.2 Non-covalent interactions within the coacervates

Next, we systematically investigated the nature of the interactions between ATP and PHMB using a combination of spectroscopic and physico-chemical techniques. We began by performing  $^{31}\text{P}$  nuclear magnetic resonance (NMR) spectroscopy on ATP in the presence of PHMB. Distinct changes in the chemical shift of the  $\alpha$ ,  $\beta$ , and  $\gamma$  phosphate peaks of ATP were observed in the NMR spectrum upon coacervate formation (Fig. 2b). Notable upfield chemical shifts of the  $\alpha$ -P from  $-11.26$  to  $-11.30$ ,  $\beta$ -P from  $-22.91$  to  $-22.98$ , and  $\gamma$ -P from  $-10.72$  to  $-10.76$  of ATP (Fig. 2a) in the presence of PHMB highlight the molecular interactions between the phosphates of ATP and biguanide moieties of PHMB.<sup>64</sup> We measured the zeta potential of PA-Coa across various ATP-to-PHMB ratios to confirm the importance of electrostatic interactions in PA-Coa formation (Fig. 2b). The zeta potential decreased gradually from approximately  $+55\text{ mV}$  to near-neutral values as the ATP-to-PHMB ratio increased from 0.5 to 2.0, demonstrating neutralization of the positive charges of PHMB by negatively charged ATP molecules, thereby promoting LLPS. Beyond a critical ATP concentration, however, charge overcompensation occurred, resulting in a net

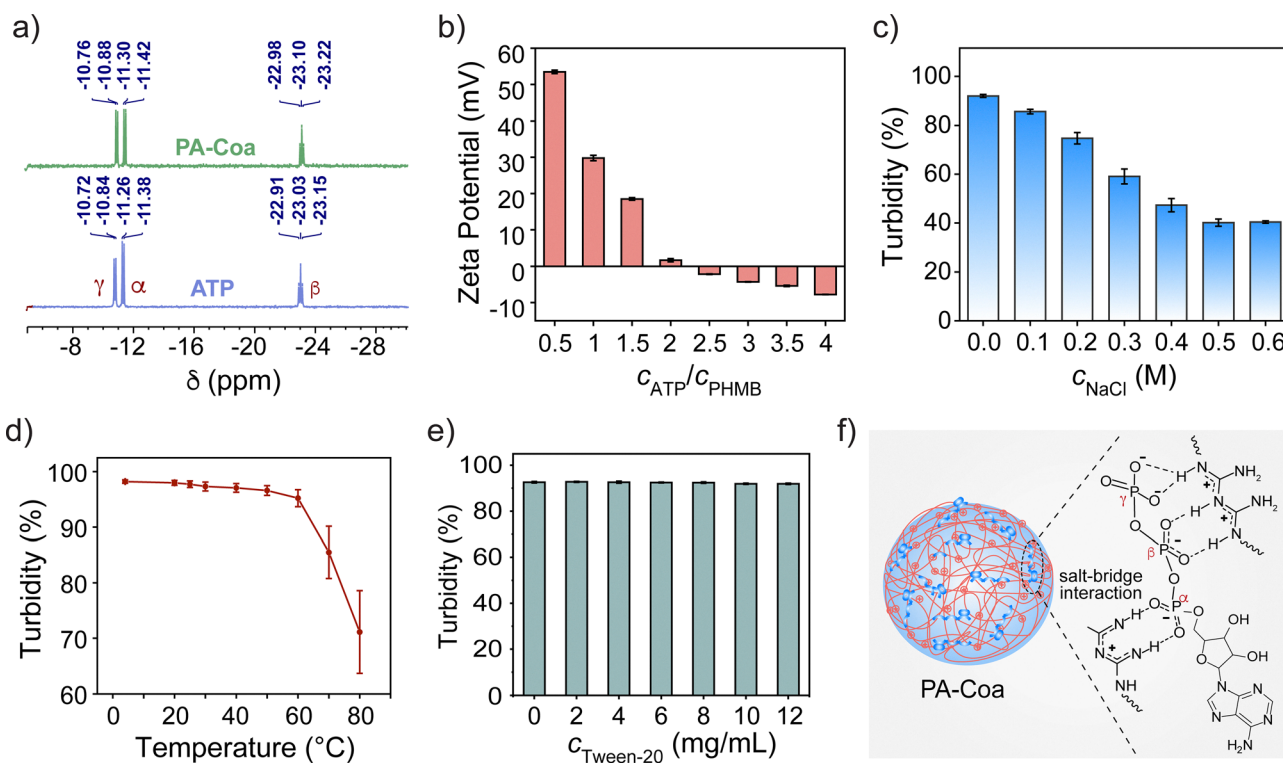


Fig. 2 Molecular interactions responsible for PA-Coa formation. (a)  $^{31}\text{P}$ -NMR spectra comparing free ATP (bottom, blue) with ATP incorporated in PA-Coa (top, green). The chemical shifts corresponding to the  $\gamma$ ,  $\alpha$ , and  $\beta$  phosphates are slightly shifted upon complexation with PHMB, indicating interaction and binding within the coacervate phase. (b) Zeta potential of ATP/PHMB mixtures at varying ratios, with PHMB concentration in  $\text{mg mL}^{-1}$  and ATP in  $\text{mM}$ . (c) Effect of increasing  $\text{NaCl}$  concentration on the turbidity of the solution, indicating disruption of electrostatic interactions and destabilization of the coacervates. (d) Thermal stability profile of PA-Coa showing a sharp turbidity drop above  $50\text{ }^\circ\text{C}$ , suggesting temperature-responsive disassembly likely due to the disruption of hydrogen bonding and weakening of electrostatic interactions at elevated temperatures. (e) The turbidity of PA-Coa remains unchanged in the presence of increasing concentrations of Tween-20, suggesting minimal contribution of hydrophobic interactions to coacervate stability. (f) Schematic representation of plausible non-covalent interactions leading to coacervate formation between PHMB and ATP highlighting key salt-bridge interactions between the biguanide and the phosphate moieties. The error bars depict the standard deviations calculated from three technical replicates.

negative surface charge. This negative surface potential increased electrostatic repulsions, ultimately leading to destabilization of the coacervate phase. We further assessed the stability of PA-Coa in the presence of various competitive media. We investigated how ionic strength affected the structural integrity of PA-Coa. A steady decline in turbidity with the gradual addition of NaCl (Fig. 2c) strongly implicated electrostatic interactions as a critical structural component of the assemblies.

Next, we examined the thermal stability of the coacervates to assess their robustness at physiologically relevant and elevated temperatures. The turbidity of the coacervate solution stayed almost constant up to 50 °C (Fig. 2d), but the coacervate network quickly destabilized above 50 °C, indicated by the sharp drop in turbidity beyond this point. We further investigated the effect of guanidinium hydrochloride (Gua.HCl), a known chaotropic agent,<sup>62</sup> on the integrity of PA-Coa. Increasing concentrations of Gua.HCl led to progressive dissolution of the coacervates, as evidenced by a corresponding decrease in turbidity (Fig. S9). Together, both the effect of higher temperature and Gua.HCl clearly demonstrates that the stability of PA-Coa critically depends on these non-covalent interactions, particularly hydrogen bonds and electrostatic attractions,<sup>65</sup> which play a major role in coacervate formation. Next, we tested the resistance of PA-Coa to Tween-20, a non-ionic surfactant. As shown in Fig. 2e, turbidity remained consistent as the concentration of Tween-20 increased from 0 to 12 mg mL<sup>-1</sup>.<sup>66</sup> This minimal response suggests that hydrophobic interactions play a limited role in maintaining the stability of the PA-Coa structure. Altogether, these findings reveal that PA-Coa formation is primarily driven by salt-bridge interactions between ATP and PHMB, resulting in dynamic assemblies that are both responsive and stable under selective conditions. As schematically illustrated in Fig. 2f, the coacervate interior likely consists of a heterogeneous, ionically crosslinked network, providing a versatile environment for cargo retention. Therefore, we decided to encapsulate the anionic G-quadruplex (GQ) structure within the coacervates to leverage this platform for its potential in responsive and adaptive applications.

### 2.3 Incorporation of GQ-DNA within PA-Coa

Compartmentalization plays an important role in biological systems for segregating biochemical pathways and enhancing the activity of enzymes by creating a confined environment. Inspired by this feature of biological systems, we aimed to incorporate G-rich sequences that form GQ within PA-Coa to ultimately study how DNAzymes behave inside cells and how their activity gets modulated by exploiting the adaptable and non-equilibrium nature of such systems.<sup>67</sup> We also expected that the incorporation of GQ structures within coacervates would reduce the internal fluidity and enhance molecular crowding, factors that could in turn modulate the material properties and functional behavior of these coacervates. A guanine-rich GQ-DNA sequence (5'-CGGGCGGGCGCGAGG-GAGGG-3') spontaneously folded into a GQ structure upon the addition of potassium ions, which promote Hoogsteen-type

hydrogen bonding and stabilize the quadruplex formation (Fig. 3a).<sup>68</sup> This switch in conformation was validated by circular dichroism (CD) spectroscopy, revealing a positive peak at ~265 nm and a negative peak at ~240 nm, which are characteristic of a parallel GQ topology. Importantly, CD spectroscopy further confirmed that the GQ-DNA retained its structural integrity within the GQ-PA-Coa microenvironment as observed from the unaltered CD peaks similar to the free GQ-DNA (Fig. 3b).

GQ-DNA was subsequently incorporated into PA-Coa, resulting in the formation of a hybrid coacervate system termed as GQ-PA-Coa (Fig. 3c). We introduced a dye labelled GQ-DNA (FAM-GQ) into PA-Coa to examine the extent of GQ enrichment within the coacervate droplets.<sup>69</sup> As shown in Fig. 3d, GQ-PA-Coa exhibited uniform fluorescence intensity throughout the coacervate. The 3D z-stack images further confirmed complete delocalization of GQ-DNA within the internal volume, indicating uniform distribution inside the coacervate (Fig. 3d). We further studied the dynamic behavior of the condensed phase of GQ-PA using FRAP. Compared to PA-Coa, GQ-PA-Coa exhibited significantly slower fluorescence recovery. Within 80 seconds, only ~40% fluorescence was recovered in GQ-PA-Coa, in contrast to >80% recovery observed in PA-Coa (Fig. 3e and f, and Fig. S10). This significant reduction in recovery indicates decreased molecular mobility, likely resulting from enhanced molecular crowding and restricted diffusion caused by GQ incorporation. To quantify the diffusion, we calculated the diffusion coefficients ( $D$ ) for both PA-Coa and GQ-PA-Coa using the Sompasis equation,<sup>70</sup> a well-accepted model for analysing the diffusion-modulated kinetics of fluorescence recovery (Table S1). The equation is as follows:

$$D = \frac{0.224r^2}{\tau_{1/2}}$$

where  $D$  is the diffusion coefficient,  $r$  is the radius of the bleached region, and  $\tau_{1/2}$  is the half-time of fluorescence recovery. The estimated  $D$  for GQ-PA-Coa ( $0.87 \times 10^{-3} \mu\text{m}^2 \text{s}^{-1}$ ) was lower than that of PA-Coa ( $4.12 \times 10^{-3} \mu\text{m}^2 \text{s}^{-1}$ ), validating that GQ incorporation reduces molecular mobility. This indicates a clear transition of the coacervate to a denser and more crowded internal environment,<sup>71,72</sup> driven by the formation of a self-assembled GQ-DNA structure inside PA-Coa. The high local concentration of GQ motifs and restricted diffusion can serve as a platform to spatially confine and stabilize catalytic centers, enhancing the reaction efficiency through molecular crowding effects.

### 2.4 GQ-PA-Coa as DNAzyme-mimetic catalytic compartments

GQ structures are known to interact with cofactors such as hemin to form GQ-hemin DNAzymes, which mimic peroxidase enzymes.<sup>73</sup> We hypothesized that embedding these catalytic motifs within a condensed and molecularly crowded matrix of PA-Coa would significantly enhance substrate retention and elevate local reaction rates, similar to biomolecular condensates.<sup>8</sup> The GQ-hemin DNAzyme efficiently oxidizes the 2,2'-azino-bis(3-ethylbenzothiazoline-6-sulfonic acid) (ABTS) substrate to its oxidized form of ABTS<sup>•+</sup> (ABTS<sub>ox</sub>) (Fig. 4a).<sup>74</sup>

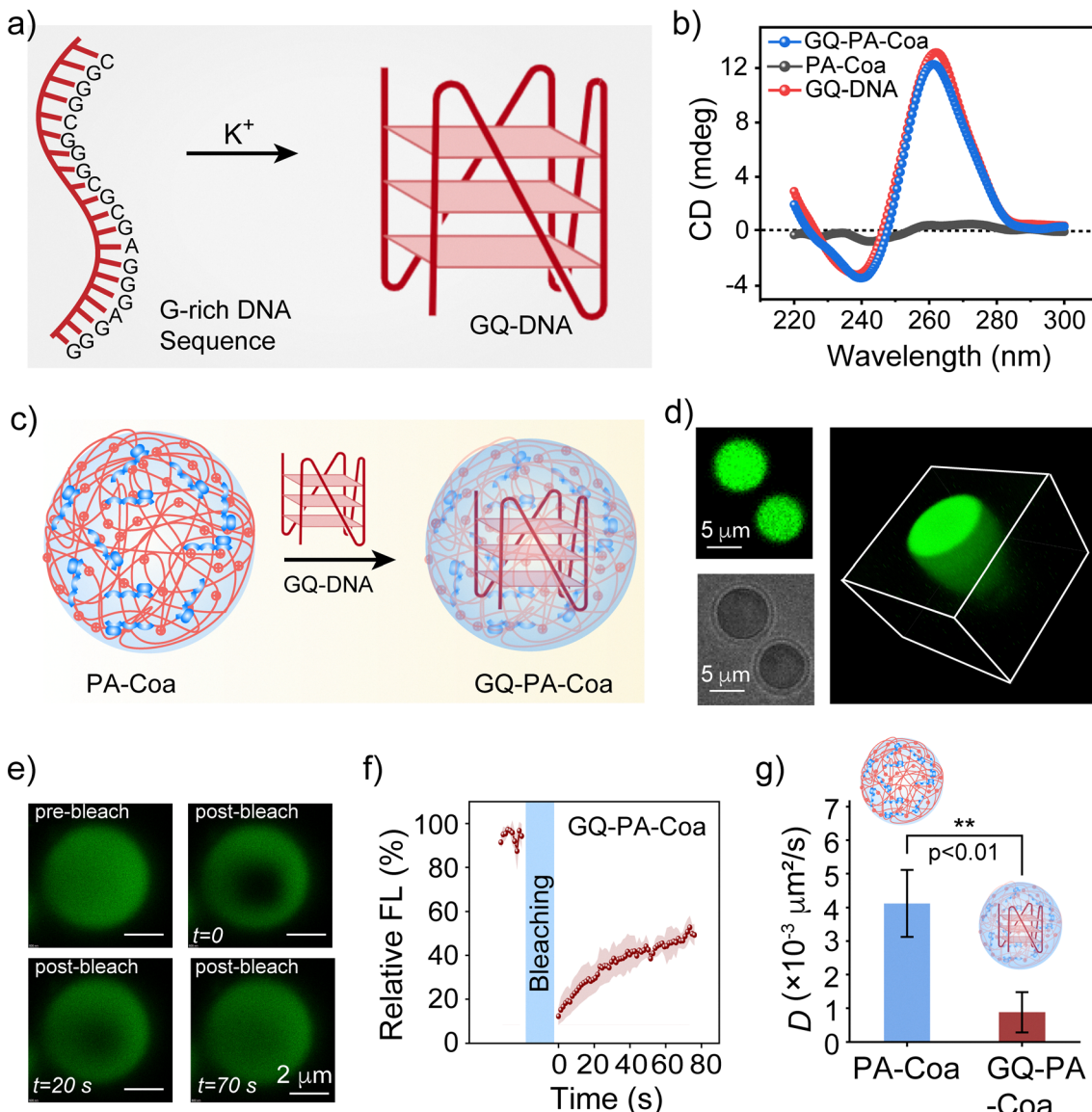


**Fig. 3** Incorporation of G-quadruplex forming DNA into PA-Coa. (a) A G-rich single-stranded DNA sequence undergoes conformational changes in the presence of  $K^+$  to form a GQ-DNA. (b) Circular dichroism spectra showing the characteristic peaks of parallel G-quadruplex DNA, which are retained even in the presence of PA-Coa. (c) Schematic showing the integration of GQ-DNA into PA-Coa to form GQ-PA composite coacervates. (d) CLSM and bright-field images showing the localization of GQ-DNA within PA-Coa using FAM-labeled GQ-DNA (green fluorescence). The 3D reconstruction further illustrates the homogeneous distribution of FAM-labelled GQ-DNA throughout the interior of the coacervate. (e) FRAP images of GQ-PA-Coa showing fluorescence recovery over time. (f) The relative fluorescence (FL) recovery curve shows reduced and slower fluorescence recovery in GQ-PA-Coa, indicating hindered molecular diffusion due to GQ-DNA incorporation ( $n = 3$ , independent experiments; mean  $\pm$  SD). (g) Comparison of diffusion coefficients ( $D$ ) in PA-Coa and GQ-PA-Coa, showing significantly reduced diffusion in the GQ-containing system.

We carried out activity assays by monitoring the oxidation of ABTS spectrophotometrically at 418 nm. The highest catalytic activity ( $\sim 0.83 \mu\text{M min}^{-1}$ ) was clearly observed when all the components, including GQ-Coa, hemin,  $\text{H}_2\text{O}_2$ , and ABTS, were simultaneously present (Fig. 4b), highlighting the best performance of the DNAzyme inside the PA-Coa compartments. In contrast, substantially reduced activities were recorded under conditions where individual components were absent. Specifically, a  $\sim 10$ -fold decrease in catalytic activity ( $0.08 \mu\text{M min}^{-1}$ ) was observed in the absence of PA-Coa (control 6, Fig. 4b) despite the presence of all other components, highlighting the

role of confinement for the catalysis. Also, hemin without the GQ encapsulation (PA-Coa +  $\text{H}_2\text{O}_2$  + ABTS) led to a 2-fold reduction in catalytic efficiency ( $\sim 0.42 \mu\text{M min}^{-1}$ ) inside the coacervate, indicating the importance of GQ-DNA as a scaffold for effective hemin binding and catalysis (Fig. 4b). This decrease in activity also aligns with the previously noted reduction in the diffusion coefficient within GQ-PA-Coa (Fig. 3g), emphasizing that molecular crowding impacts the catalytic efficiency through enhanced local reactant concentration and controlled diffusion dynamics. Likewise, other control reactions missing either hemin,  $\text{H}_2\text{O}_2$ , or ABTS yielded

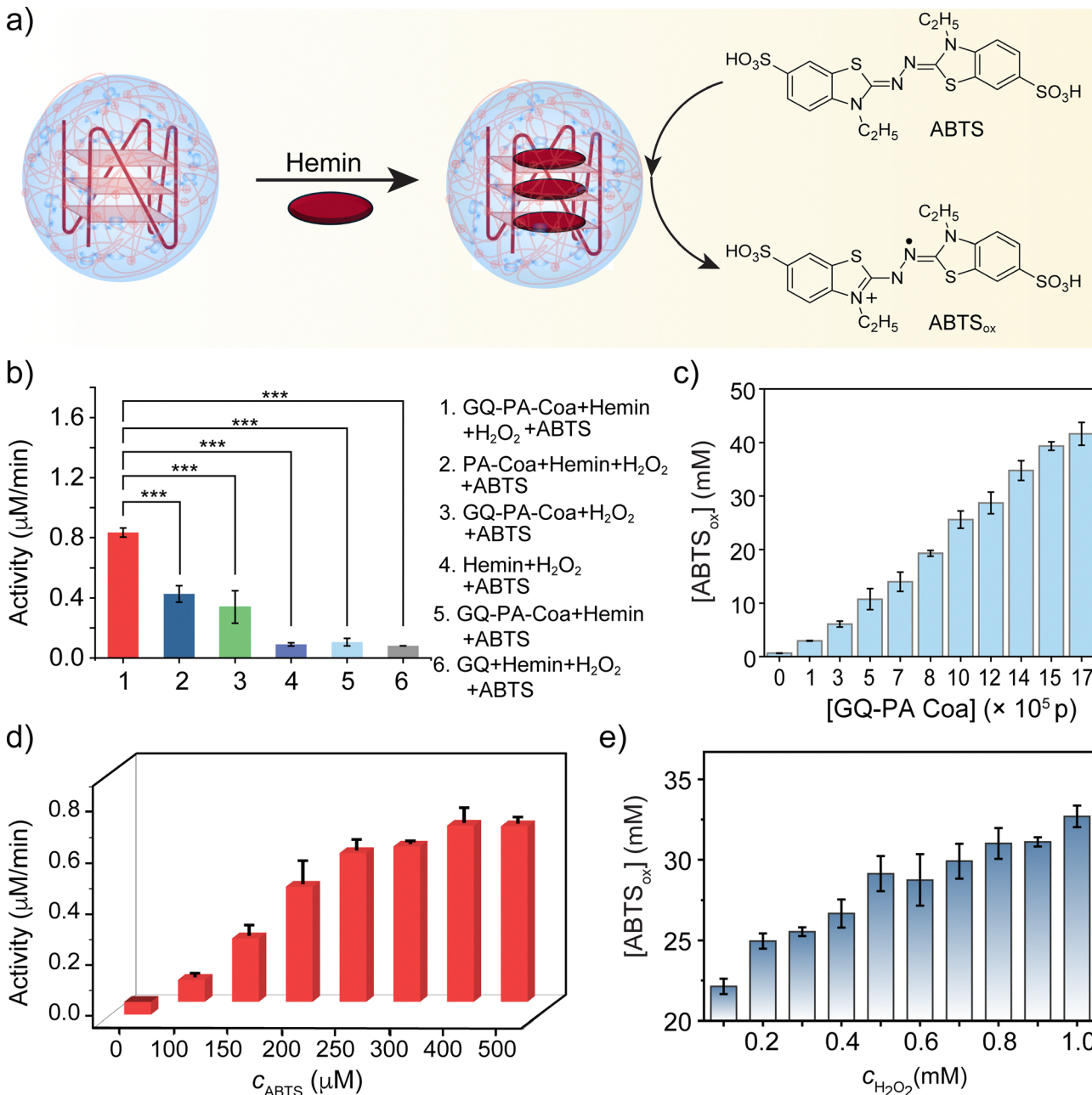


**Fig. 4** GQ-PA-Coa exhibits enhanced peroxidase-like catalytic activity. (a) Schematic representation of GQ structures in the presence of potassium ions ( $K^+$ ). (b) Peroxidase-like activity of hemin encapsulated GQ-PA-Coa, demonstrating significantly enhanced catalytic activity when hemin is co-localized with GQ-DNA within coacervates. The values represent mean  $\pm$  standard deviation,  $n = 3$ . Statistical significance was calculated by an unpaired  $t$ -test; \*\*\* $p < 0.001$ . (c) Product (oxidized ABTS) concentration with increasing GQ-PA-Coa concentration, showing a dose-dependent increase in catalytic output.  $p$  represents the number of particles, as calculated from FACS. (d) Dependence of catalytic activity on ABTS concentration, showing saturation kinetics typical of enzyme-like behavior. (e) Activity dependence on  $H_2O_2$  concentration, also demonstrating a dose-dependent increase in catalytic activity. The error bars represent the standard deviations from three technical replicates.

even lower rates (Fig. 4b, and Fig. S11), confirming that the complete Hemin-GQ-PA-Coa assembly is essential for optimal peroxidase-mimetic activity.

Next, we carried out catalytic assays using varying concentrations of the Hemin-GQ-PA-Coa assembly while maintaining constant substrate (1 mM ABTS and 1 mM  $H_2O_2$ ) to investigate the dose-dependent catalytic behavior of the system. To

correlate activity with the number of active coacervate particles, fluorescence-activated cell sorting (FACS) analysis was used (Fig. S12). The results showed a clear linear increase in product formation ( $ABTS^{*}$ ) after 60 minutes, as the concentration of Hemin-GQ-PA-Coa increased (Fig. 4c and Fig. S13). This linear correlation suggests that the catalytic activity scales proportionally with the amount of active DNAzyme-loaded coacervate,

further supporting the role of the confined GQ-hemin system as an efficient and tunable peroxidase-mimetic catalyst. Following this, we investigated the effect of varying the concentration of ABTS within the Hemin-GQ-PA-Coa system. As the ABTS concentration increased, a corresponding and significant enhancement in catalytic activity was observed (Fig. 4d and Fig. S14). This increase suggests that the system exhibits substrate-responsive properties. The kinetic data fit well to the Michaelis–Menten model, confirming classic saturation kinetics (Fig. S15). Fitting the curve to this model yielded a Michaelis constant  $K_M$  of 621  $\mu\text{M}$  and a maximum reaction velocity  $V_{\text{max}}$  of 1.76  $\mu\text{M min}^{-1}$  for the Hemin-GQ-PA-Coa system. A similar trend was observed with varying  $\text{H}_2\text{O}_2$  concentrations, where higher levels resulted in increased product formation (Fig. 4e and Fig. S16). These findings suggest that the GQ-PA-Coa system enhances the reaction kinetics by concentrating substrates, optimizing their orientation, and facilitating activation within the confined microenvironment. Notably, the GQ-PA-Coa system exhibits  $\sim 2$ -fold higher catalytic efficiency compared to free Hemin in coacervates, likely due to the higher-order assembly and enhanced structural organization of Hemin within the GQ structure. This underscores the

potential of such coacervate-based systems as versatile platforms for mimicking primitive enzymatic activity in protocell models.

## 2.5 Transient PA-Coa regulated DNAzyme activity

Cellular function in living systems is dynamically regulated by biomolecular condensates, formed through phase separation.<sup>75</sup> These energy-dependent structures self-organize *via* reversible macromolecular interactions and are highly responsive to changes in their environment.<sup>76</sup> Importantly, their formation and breakdown are often tightly regulated by energy-dependent mechanisms, allowing for precise spatial and temporal control of the biochemical reactions that take place inside such condensates.<sup>10</sup> Thus, the non-equilibrium nature of these condensates is important for the modulation of reaction rates and chemical activities as per the demands of the cell, impacting the metabolome and various cellular processes. To achieve an energy dissipation-based coacervate system, we programmed the dissolution of PA-Coa by enzymatically degrading ATP, which is a core component of the coacervate (Fig. 5a). We utilized ALP to enzymatically hydrolyze ATP into adenosine and inorganic phosphates (Pi). Control experiments confirmed that

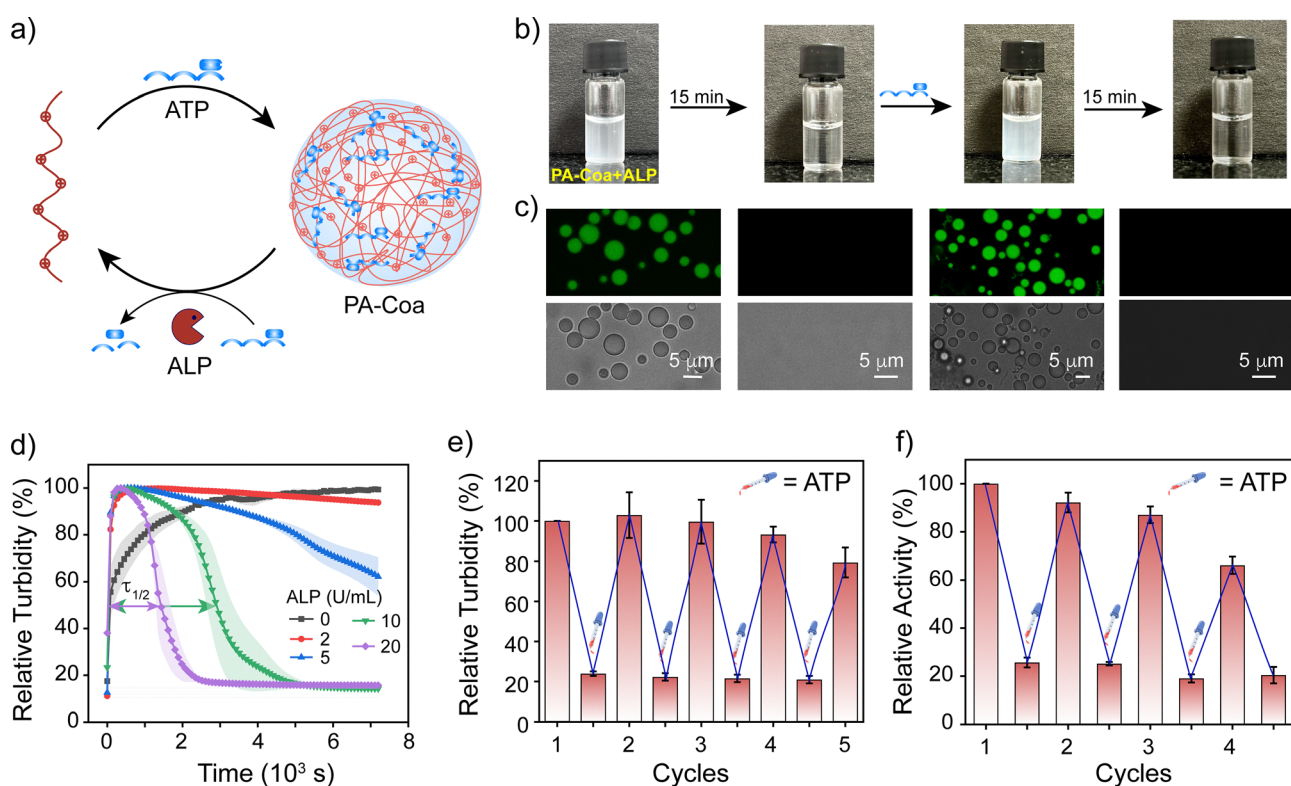


Fig. 5 ATP-driven reversible formation and enzymatic disassembly of PA-Coa, enabling dynamic activity cycling. (a) Schematic of ATP-induced PA-Coa formation, and subsequent enzymatic disassembly by ALP through ATP hydrolysis. (b) Digital images demonstrating the visual transition between coacervate (turbid) and dissolved (clear) states upon the sequential addition of ATP over 15-minute intervals. ALP is present from the beginning, continuously breaking down ATP. (c) CLSM and bright-field microscopy images showing droplet formation upon ATP addition, disappearance after ALP treatment, and reformation upon subsequent ATP addition. (d) Normalized turbidity over time showing the initial formation of coacervates and their subsequent disassembly at different ALP concentrations. (e) Reversible turbidity changes over five cycles, demonstrating ALP–ATP feedback-controlled assembly-disassembly of PA-Coa. (f) Control of the activity of Hemin-GQ-PA-Coa through an ATP–ALP feedback mechanism. The pH of the medium was maintained in 100 mM Tris-HCl buffer (pH 9.0). The error bars indicate the standard deviations derived from  $n = 3$  technical replicates.

ALP alone could not induce phase separation with positively charged PHMB (Fig. S17), indicating that ALP does not participate in the coacervation. Reversible coacervate formation was directly observable through macroscopic turbidity changes. Digital images of the sample vials clearly demonstrate the dynamic nature of the system: a rapid increase in turbidity upon ATP addition indicates the formation of coacervate droplets, while a gradual return to transparency reflects their dissolution following ATP hydrolysis by ALP (Fig. 5b and Fig. S18). These visually observable transitions between turbid and clear states closely align with the underlying microscale phase behavior, directly correlating with the reversible assembly and disassembly of the coacervate. CLSM imaging with FITC dye and bright field imaging further validated the morphology of the droplets and confirmed their reversible appearance/disappearance across cycles (Fig. 5c).

In the absence of ALP, well-defined coacervate droplets remained intact over time. The addition of ALP triggered complete droplet dissolution, emphasizing the dependence of phase separation on intact ATP molecules. To evaluate the tunability of our system, we varied the ALP concentrations (from 2–20  $\text{U mL}^{-1}$ ) and monitored coacervate disassembly through turbidity measurements. As illustrated in Fig. 5d, increasing ALP levels accelerated ATP hydrolysis, thereby reducing the coacervate lifetime. Specifically, the half-life of the PA-Coa droplets decreased from 48 min to 24 min as the ALP concentration increased from 10  $\text{U mL}^{-1}$  to 20  $\text{U mL}^{-1}$  (Fig. 5d), confirming enzyme-dose-dependent control over phase behavior. With the initial dosing of 20  $\text{U mL}^{-1}$  ALP, the system sustained five successive cycles of reversible coacervate formation and dissolution. Over these cycles, a slight dampening in the coacervation was observed, which may be attributed to the gradual accumulation of the products of ATP hydrolysis, such as AMP and/or Pi (Fig. 5e).

In biological cells, membraneless condensates concentrate reactants and finely tune enzymatic reaction rates, then dissolve once the reaction is complete to self-limit their activity.<sup>77,78</sup> To mimic this behavior, we employed the peroxidase-like oxidation of ABTS, using the Hemin-GQ-PA-Coa droplets. As ALP gradually hydrolyzed ATP, the droplets disassembled, and the catalytic activity fell to around 30% of the initial value. Subsequently, a second ATP pulse led to reformation of the coacervate droplets and concomitant increase in ABTS oxidation to around 92% of the initial activity, demonstrating reversible “on-off” control of peroxidase-like activity. We successfully cycled this assembly and disassembly process four times (Fig. 5f). Although a slight decrease in the restored activity was observed over these cycles (retaining ~66% by the fourth cycle) by adding the same equivalent of ATP. We attribute the activity decay primarily to two factors: (i) a significant decrease in pH from inorganic phosphate accumulation during ATP hydrolysis, which suppresses the peroxidase-like activity of hemin,<sup>79</sup> and (ii) interactions between accumulating monophosphates and the guanidine groups of PHMB, reducing their availability for re-coacervation. Table S2 quantitatively demonstrates the pH decrease in

the unbuffered aqueous medium, where the pH dropped to 3.40 and the activity declined to ~34% at the end of the fourth cycle (Fig. S19). In contrast, the 100 mM Tris-HCl buffer (pH 9.0) effectively mitigated this effect, maintaining a pH of 7.20 after the fourth cycle, which correlated with markedly improved activity retention (Fig. 5f). The residual decay that persists even under these optimized buffered conditions is attributable to the gradual accumulation of monophosphates and their competitive interactions with the guanidine moieties of PHMB. Collectively, these results demonstrate a fuel-dependent transient coacervate system offering programmable control over both phase segregation and biocatalytic function *via* sustained energy consumption. The resultant out-of-equilibrium dynamics enable fine mimicry of the tunable and adaptive characteristic of biomolecular condensates. On a practical note, the salt-bridge mediated PA-Coa displays great stability in biorelevant media such as 10% fetal bovine serum (Fig. S20), showing promise of the system in future biomedical applications.

### 3. Conclusions and future scope

In summary, we developed a transient coacervate system driven by multivalent salt-bridge interactions between biguanidine units and phosphate groups. This system uptakes GQ-DNA to create a spatially confined catalytic nanoreactor. Such synergistic integration generates microenvironments in which GQ nanostructures serve as optimized scaffolds for effective hemin stacking and binding. The coacervate phase selectively sequesters the GQ-hemin catalytic core along with its substrates, leading to significantly enhanced catalytic performance compared to non-compartmentalized systems. This approach demonstrates that coupling phase separation with molecular self-assembly is a powerful strategy for constructing biomimetic enzymatic organelles. Furthermore, PA-Coa’s fuel-driven, dissipative assembly-disassembly cycles yield a tunable system whose lifetime can be precisely controlled. These responsive droplets serve not only as hosts for the catalytic machinery but also as versatile microreactors for GQ-hemin chemistry. By uniting molecular concentration with controllable dynamics, this coacervate platform enables robust, droplet-based catalysis.

Our results provide compelling evidence that emergent functionality, specifically augmented catalysis, arises directly from the spatial organization and confinement within these small compartments. This work advances the fundamental understanding of how complex chemical behaviors can evolve from controlled hierarchical organization in non-equilibrium environments. It establishes a robust, adaptable platform for developing next-generation synthetic organelles and responsive catalytic systems, bridging disciplines from synthetic biology and systems chemistry to soft materials science. Collectively, these findings pave the way for designing adaptive chemical networks including DNA nanostructures with life-like properties.

## Conflicts of interest

The authors declare no competing financial interest.

## Data availability

All the data that support this study are included in this article and its SI. The Supplementary Information file includes details of materials and instrumentation, experimental procedures, phase diagrams, methodology of optical microscopy, FRAP, sample preparation for NMR, zeta potential, and dynamic light scattering studies. It also contains protocols for fluorescence imaging, dye encapsulation, catalytic activity assays, and additional figures and tables supporting the main text. See DOI: <https://doi.org/10.1039/d5nh00519a>.

## Acknowledgements

This work was financially supported by Science and Engineering Research Board (CRG/2022/009021) and Department of Biotechnology (BT/PR49984/MED/32/911/2023). A. S. is thankful to the Prime Minister's Research Fellowship for doctoral research. P. K. thanks DST for the KVPY-INSPIRE fellowship. M. P. is thankful to the Ministry of Education for the doctoral fellowship. S. D. acknowledges Department of Biotechnology for the financial support through the DBT-RA Program in Biotechnology and Life Sciences.

## References

- 1 T. Misteli, *J. Cell Biol.*, 2001, **155**, 181–186.
- 2 A. Chaudhuri, B. Bhattacharya, K. Gowrishankar, S. Mayor and M. Rao, *Proc. Natl. Acad. Sci. U. S. A.*, 2011, **108**, 14825–14830.
- 3 G. Laflamme and K. Mekhail, *Commun. Biol.*, 2020, **3**, 773.
- 4 M.-T. Wei, Y.-C. Chang, S. F. Shimobayashi, Y. Shin, A. R. Strom and C. P. Brangwynne, *Nat. Cell Biol.*, 2020, **22**, 1187–1196.
- 5 S. Alberti and A. A. Hyman, *Nat. Rev. Mol. Cell Biol.*, 2021, **22**, 196–213.
- 6 H. Li, C. Leo, J. Zhu, X. Wu, J. O'Neil, E.-J. Park and J. D. Chen, *Mol. Cell. Biol.*, 2000, **20**, 1784–1796.
- 7 C. Brasnett, A. Kiani, S. Sami, S. Otto and S. J. Marrink, *Commun. Chem.*, 2024, **7**, 151.
- 8 S. Lim and D. S. Clark, *Trends Biotechnol.*, 2024, **42**, 496–509.
- 9 F. D. Mast, A. V. Ratushny and J. D. Aitchison, *J. Cell Biol.*, 2014, **206**, 695–706.
- 10 S. F. Banani, H. O. Lee, A. A. Hyman and M. K. Rosen, *Nat. Rev. Mol. Cell Biol.*, 2017, **18**, 285–298.
- 11 I. A. Antifeeva, A. V. Fonin, A. S. Fefilova, O. V. Stepanenko, O. I. Povarova, S. A. Silonov, I. M. Kuznetsova, V. N. Uversky and K. K. Turoverov, *Cell. Mol. Life Sci.*, 2022, **79**, 251.
- 12 S. Boyko, X. Qi, T.-H. Chen, K. Surewicz and W. K. Surewicz, *J. Biol. Chem.*, 2019, **294**, 11054–11059.
- 13 B. Gabryelczyk, H. Cai, X. Shi, Y. Sun, P. J. M. Swinkels, S. Salentinig, K. Pervushin and A. Miserez, *Nat. Commun.*, 2019, **10**, 5465.
- 14 X. Liu, A. H. Mokarizadeh, A. Narayanan, P. Mane, A. Pandit, Y.-M. Tseng, M. Tsige and A. Joy, *J. Am. Chem. Soc.*, 2023, **145**, 23109–23120.
- 15 P. Chowdhury, B. Saha, K. Bauri, B. S. Sumerlin and P. De, *J. Am. Chem. Soc.*, 2024, **146**, 21664–21676.
- 16 X. Tong, R. Tang, J. Xu, W. Wang, Y. Zhao, X. Yu and S. Shi, *Signal Transduct. Target. Ther.*, 2022, **7**, 221.
- 17 I. Alshareedah, M. M. Moosa, M. Pham, D. A. Potoyan and P. R. Banerjee, *Nat. Commun.*, 2021, **12**, 6620.
- 18 M. C. Munder, D. Midtvedt, T. Franzmann, E. Nüske, O. Otto, M. Herbig, E. Ulbricht, P. Müller, A. Taubenberger, S. Maharana, L. Malinovska, D. Richter, J. Guck, V. Zaburdaev and S. Alberti, *eLife*, 2016, **5**, e09347.
- 19 M. Delarue, G. P. Brittingham, S. Pfeffer, I. V. Surovtsev, S. Pinglay, K. J. Kennedy, M. Schaffer, J. I. Gutierrez, D. Sang, G. Poterewicz, J. K. Chung, J. M. Plitzko, J. T. Groves, C. Jacobs-Wagner, B. D. Engel and L. J. Holt, *Cell*, 2018, **174**, 338–349.e320.
- 20 M. R. King, K. M. Ruff, A. Z. Lin, A. Pant, M. Farag, J. M. Lalmansingh, T. Wu, M. J. Fossat, W. Ouyang, M. D. Lew, E. Lundberg, M. D. Vahey and R. V. Pappu, *Cell*, 2024, **187**, 1889–1906.e1824.
- 21 S. Song, T. Ivanov, T. P. Doan-Nguyen, L. C. da Silva, J. Xie, K. Landfester and S. Cao, *Angew. Chem., Int. Ed.*, 2025, **64**, e202418431.
- 22 A. B. Cook, S. Novosedlik and J. C. M. van Hest, *Acc. Mater. Res.*, 2023, **4**, 287–298.
- 23 S. Koga, D. S. Williams, A. W. Perriman and S. Mann, *Nat. Chem.*, 2011, **3**, 720–724.
- 24 S. Rasmussen, L. Chen, M. Nilsson and S. Abe, *Artif. Life*, 2003, **9**, 269–316.
- 25 R. Booth, Y. Qiao, M. Li and S. Mann, *Angew. Chem., Int. Ed.*, 2019, **58**, 9120–9124.
- 26 S. Cao, T. Ivanov, J. Heuer, C. T. J. Ferguson, K. Landfester and L. Caire da Silva, *Nat. Commun.*, 2024, **15**, 39.
- 27 J. Yuan and H. Tanaka, *Nat. Commun.*, 2025, **16**, 1517.
- 28 D. Q. P. Reis, S. Pereira, A. P. Ramos, P. M. Pereira, L. Morgado, J. Calvário, A. O. Henriques, M. Serrano and A. S. Pina, *Nat. Commun.*, 2024, **15**, 9368.
- 29 S. L. Higashi and M. Ikeda, *Adv. Biol.*, 2025, **9**, 2400572.
- 30 D. Wang, L. Zhou, X. Zhang, Z. Zhou, Z. Huang and N. Gao, *Angew. Chem., Int. Ed.*, 2025, **64**, e202422601.
- 31 I. B. A. Smokers, B. S. Visser, A. D. Slootbeek, W. T. S. Huck and E. Spruijt, *Acc. Chem. Res.*, 2024, **57**, 1885–1895.
- 32 C. Love, J. Steinkühler, D. T. Gonzales, N. Yandrapalli, T. Robinson, R. Dimova and T.-Y. D. Tang, *Angew. Chem., Int. Ed.*, 2020, **59**, 5950–5957.
- 33 T. Lu, K. K. Nakashima and E. Spruijt, *J. Phys. Chem. B*, 2021, **125**, 3080–3091.
- 34 T.-Y. Heo and S.-H. Choi, *J. Phys. Chem. B*, 2024, **128**, 1256–1265.
- 35 J. Wang, M. Abbas, Y. Huang, J. Wang and Y. Li, *Commun. Chem.*, 2023, **6**, 243.

36 C. P. Brangwynne, C. R. Eckmann, D. S. Courson, A. Rybarska, C. Hoege, J. Gharakhani, F. Jülicher and A. A. Hyman, *Science*, 2009, **324**, 1729–1732.

37 W. D. Snyder and S. W. Fox, *Biosyst.*, 1975, **7**, 222–229.

38 M. H. M. E. van Stevendaal, L. Vasiukas, N. A. Yewdall, A. F. Mason and J. C. M. van Hest, *ACS Appl. Mater. Interfaces*, 2021, **13**, 7879–7889.

39 B. Harrow, *Science*, 1938, **88**, 58.

40 C. Qi, X. Ma, Q. Zeng, Z. Huang, S. Zhang, X. Deng, T. Kong and Z. Liu, *Nat. Commun.*, 2024, **15**, 1107.

41 C. M. Green, D. Sementa, D. Mathur, J. S. Melinger, P. Deshpande, S. Elbaum-Garfinkle, I. L. Medintz, R. V. Ulijn and S. A. Diaz, *Commun. Chem.*, 2024, **7**, 49.

42 C. Lim and W. C. Blocher McTigue, *ACS Biomater. Sci. Eng.*, 2024, **10**, 6766–6789.

43 H. Yang, X. Zhang, S. Wang, Y. Wang, R. Xiong and C. Huang, *Interdiscip. Mater.*, 2025, **4**, 539–567.

44 Y. Ji, Y. Lin and Y. Qiao, *J. Am. Chem. Soc.*, 2023, **145**, 12576–12585.

45 L. Li, S. Srivastava, M. Andreev, A. B. Marciel, J. J. de Pablo and M. V. Tirrell, *Macromolecules*, 2018, **51**, 2988–2995.

46 P. K. Pandey, A. Sathyavageeswaran, N. Holmlund and S. L. Perry, *ACS Macro Lett.*, 2025, **14**, 43–50.

47 F. Späth, C. Donau, A. M. Bergmann, M. Kränzlein, C. V. Synatschke, B. Rieger and J. Boekhoven, *J. Am. Chem. Soc.*, 2021, **143**, 4782–4789.

48 T. Lu and E. Spruijt, *J. Am. Chem. Soc.*, 2020, **142**, 2905–2914.

49 J. Wu, J. Ye, J. Zhu, Z. Xiao, C. He, H. Shi, Y. Wang, C. Lin, H. Zhang, Y. Zhao, X. Fu, H. Chen, X. Li, L. Li, J. Zheng and J. Xiao, *Biomacromolecules*, 2016, **17**, 2168–2177.

50 H. E. Cingil, N. C. H. Meertens and I. K. Voets, *Small*, 2018, **14**, 1802089.

51 R. Mogaki, K. Okuro and T. Aida, *Chem. Sci.*, 2015, **6**, 2802–2805.

52 L. T. Hao, S. Park, S. Choy, Y. M. Kim, S. W. Lee, Y. S. Ok, J. M. Koo, S. Y. Hwang, D. S. Hwang, J. Park and D. X. Oh, *JACS Au*, 2021, **1**, 1399–1411.

53 M. C. Ferrolino, D. M. Mitrea, J. R. Michael and R. W. Kriwacki, *Nat. Commun.*, 2018, **9**, 5064.

54 S. Elbaum-Garfinkle, Y. Kim, K. Szczeponiak, C. C.-H. Chen, C. R. Eckmann, S. Myong and C. P. Brangwynne, *Proc. Natl. Acad. Sci. U. S. A.*, 2015, **112**, 7189–7194.

55 T. Mittag and R. Parker, *J. Mol. Biol.*, 2018, **430**, 4636–4649.

56 Z. Dong, Q. Luo and J. Liu, *Chem. Soc. Rev.*, 2012, **41**, 7890–7908.

57 M. Solra, R. Kapila, S. Das, P. Bhatt and S. Rana, *Angew. Chem., Int. Ed.*, 2024, **63**, e202400348.

58 L. M. Larcher, I. L. Pitout, N. P. Keegan, R. N. Veedu and S. Fletcher, *Nucleic Acid Ther.*, 2023, **33**, 178–192.

59 S. Das, M. Solra, J. Sahoo, A. Srivastava, S. Fathima, M. De and S. Rana, *Chem. Mater.*, 2024, **36**, 759–771.

60 D. Rhodes and H. J. Lipps, *Nucleic Acids Res.*, 2015, **43**, 8627–8637.

61 Q. Wang, Z. Yang, X. Zhang, X. Xiao, C. K. Chang and B. Xu, *Angew. Chem., Int. Ed.*, 2007, **46**, 4285–4289.

62 R. F. Greene, Jr. and C. N. Pace, *J. Biol. Chem.*, 1974, **249**, 5388–5393.

63 M. Ghahremani Nasab, L. Hassani, S. Mohammadi Nejad and D. Norouzi, *J. Biol. Phys.*, 2017, **43**, 5–14.

64 A. Kamra, S. Das, P. Bhatt, M. Solra, T. Maity and S. Rana, *Chem. Sci.*, 2023, **14**, 9267–9282.

65 G. C. Pimentel and A. L. McClellan, *Annu. Rev. Phys. Chem.*, 1971, **22**, 347–385.

66 M. Carafa, C. Marianecchi, G. Lucania, E. Marchei and E. Santucci, *J. Control. Release*, 2004, **95**, 67–74.

67 R. Liu, Y. Yun, Z.-Y. Feng, Z. Feng, W. Zhang, Y. Ye and J. Zhang, *CCS Chem.*, 2025, **0**, 1–15.

68 Y. Xue, Z.-y. Kan, Q. Wang, Y. Yao, J. Liu, Y.-h. Hao and Z. Tan, *J. Am. Chem. Soc.*, 2007, **129**, 11185–11191.

69 J. Zhang, J. Tian, Y. He, Y. Zhao and S. Zhao, *Chem. Commun.*, 2014, **50**, 2049–2051.

70 D. M. Soumpasis, *Biophys. J.*, 1983, **41**, 95–97.

71 P. Peng, D. Stosic, A. Aitblal, A. Vimont, P. Bazin, X.-M. Liu, Z.-F. Yan, S. Mintova and A. Travert, *ACS Catal.*, 2020, **10**, 6822–6830.

72 F. Gong, M. Liu, L. Gong, S. Ye, Q. Jiang, G. Zeng, X. Zhang, Z. Peng, Y. Zhang, S. Fang and J. Liu, *Adv. Funct. Mater.*, 2022, **32**, 2202141.

73 W. Li, Y. Li, Z. Liu, B. Lin, H. Yi, F. Xu, Z. Nie and S. Yao, *Nucleic Acids Res.*, 2016, **44**, 7373–7384.

74 J. N. Rodríguez-López, D. J. Lowe, J. Hernández-Ruiz, A. N. P. Hiner, F. García-Cánovas and R. N. F. Thorneley, *J. Am. Chem. Soc.*, 2001, **123**, 11838–11847.

75 C. Garcia-Cabau and X. Salvatella, *Curr. Opin. Cell Biol.*, 2021, **69**, 111–119.

76 S. Jeon, Y. Jeon, J.-Y. Lim, Y. Kim, B. Cha and W. Kim, *Signal Transduction Targeted Ther.*, 2025, **10**, 4.

77 R. Harris, S. Veretnik, S. Dewan, A. Baruch Leshem and A. Lampel, *Commun. Chem.*, 2024, **7**, 90.

78 E. H. Brumbaugh-Reed, Y. Gao, K. Aoki and J. E. Toettcher, *Nat. Commun.*, 2024, **15**, 6717.

79 R. López-Domene, A. Manteca, A. Rodriguez-Abetxuko, A. Beloqui and A. L. Cortajarena, *Chemistry*, 2024, **30**, e202303254.